Sensors and Actuators A 295 (2019) 133–140

Contents lists available at ScienceDirect

Sensors and Actuators A: Physical

journal homepage: www.elsevier.com/locate/sna

Highly-sensitive potassium-tantalum-niobium oxide humidity sensor

Ravikant[a,b], Sheshamani Singh[a,c], Gaurav Gupta[a], Sanjay Yadav[a,b], P.K. Dubey[a,b], V.N. Ojha[a,b], Ashok Kumar[a,b,*]

[a] CSIR-National Physical Laboratory, Dr. K. S. Krishnan Marg, New Delhi 110012, India
[b] Academy of Scientific and Innovative Research (AcSIR), CSIR-National Physical Laboratory (CSIR-NPL) Campus, Dr. K. S. Krishnan Road, New Delhi 110012, India
[c] Department of Physics, Amity School of Applied Sciences (ASAS), Amity University Rajasthan, NH-11C, Jaipur- Delhi National Highway, RIICO Industrial Area, Kant Kalwar, Jaipur Rajasthan, 302006, India

ARTICLE INFO

Article history:
Received 25 February 2019
Received in revised form 28 April 2019
Accepted 15 May 2019
Available online 22 May 2019

Keywords:
Humidity sensor
Relative humidity
Ferroelectrics
Resistance

ABSTRACT

We report moisture sensitive properties of ferroelectric niobium-rich potassium tantalate $K[(Ta_{0.2}Nb_{0.8})_{0.99}Mn_{0.01}]O_3$ (KTN) which shows giant humidity response with excellent reproducibility and repeatability of data as a function of exposure time and humidity contents. Many fold change in resistance was observed with change in the relative humidity (Rh) from 15% to 95% which provides maximum sensitivity ($\bar{4}600$) at 298 K in the presence of Rh 95%. It also shows polarity dependent change in resistance with nearly 310 to 513 mV in-built potential depending on the device configuration. The polar KTN humidity sensor shows a decrease in resistance with an increase in Rh% which favors the Grotthuss mechanism responsible for humidity effects. To improve the sensitivity, a particular device configuration has implemented for the homogeneous interaction of the water vapor molecule with a maximum active sensor-surface area. The electronics with the digital display unit was designed and developed to represent the relative humidity in the form of digital display.

1. Introduction

The environmental conditions are the key for production and maintenance of industrial goods and quality of state of the art research and development at various academic institutions and research laboratory. Among various parameters, the relative humidity is one of the key parameters which maintain the quality of living and non-living things. The monitoring of humidity control plays a critical role in industrial, agricultural, food safety, medical and human day to day works [1–3]. As of today's growing need, many National Metrology Institute (NMI) had developed a primary and secondary standard for the humidity monitoring and device calibration set up [4,5]. The researchers are working on the various nanomaterials, semiconductor thin films [6], ceramics [7–9], carbon-based materials [10,11], polymers [12] and their composites, etc. for the development of the humidity sensor. The performance of these sensors is quite good, but they involved the expansive production cost, complicated and uncontrolled synthesis processes and utterly dependent on the sophisticated equipment. Many potential ceramic materials have been studied as a sensor and transducer and also for the detection of the humidity; however, they show limitation as real device applications. The main properties of a humidity sensor are high sensitivity, broad detection range, long term repeatability, low noise, fast recovery time, long lifetime and low cost. The mechanism and microelectronics of the sensors work on the two properties, i.e. (i) the change in the capacitance as a function of relative humidity (Rh), (ii) change in the resistance as a function of Rh.

Over the past few decades, efforts have done by scientific communities to develop and improve the sensing ability of the humidity sensor [3]. The SnO_2 is a semiconducting material which widely used for humidity detection [13,14]. *Qin Kuang et al.* have synthesized the SnO_2 nanowire and nanobelt using the vapor-liquid-solid technique, which has a large number of the oxygen vacancy on its surface and shows the sensitivity to 35 [15]. *Hwai-En Lin et al.* synthesized the transparent and crystalline SnO_2 film on non-seeded glass and PET substrate. They show the ratio of humidity sensing response and recovery time was 51/38 seconds for glass and 69/47 seconds for PET substrate [14]. Nowadays carbon-based nanomaterials and composites are also playing a crucial role in the fabrication of humidity sensor and actuator [16–18]. Currently, graphene oxide also attracted significant attention as an excellent nanomaterial for

* Corresponding author at: CSIR-National Physical Laboratory, Dr. K. S. Krishnan Marg, New Delhi 110012, India.
E-mail address: ashok553@nplindia.org (A. Kumar).

https://doi.org/10.1016/j.sna.2019.05.023
0924-4247/

the full range humidity, which is mainly due to its large surface area and high chemical stability. *Dongzhi Zhang et al.* describe the nanocomposite film of the tin oxide and reduced graphene oxide. They claimed that the sensor works in the wide range of the humidity from 11% to 95% and shows the sensitivity around 1570.

We report the fabrication and functional properties of novel ferroelectric ceramic KTN as a humidity sensor. The physical and chemical properties of the humidity sensor were verified with the various microstructural and electrical characterizations. The humidity response of the sensor was tested at the five different relative humidity concentrations between 15% to 95%. The sensor was further optimized for the repeatability, reproducibility, hysteresis, and stability under continuous variation of the humidity. The explanation of the humidity mechanism, detail description of the results, and verification of the structural and elemental compositions are described in the manuscript.

2. Materials and methods

The polycrystalline ceramic powder of $K[(Ta_{0.2}Nb_{0.8})_{0.99}Mn_{0.01}]O_3$ (KTN) was synthesized by the conventional solid-state reaction route. The stoichiometric ratio of potassium carbonate (K_2Co_3, 99%), niobium pentoxide (Nb_2O_5, 99.5%), tantalum pentoxide (Ta_2O_5, 99%), and manganese dioxide (MnO_2, 99.99%) (Alpha Assar) were mixed in a mortar-pestle in wet medium (isopropyl alcohol) for high homogeneity. An extra 10% potassium carbonate was added to the total ingredients to compensate for the potassium loss during high-temperature calcination and sintering processes. The mixture of ingredients was mechanically grinded in the isopropyl alcohol medium for 2 h. The blended powder was calcined at optimized temperature 900 °(±2 °) for the 2 h with the ramp period of the 5 ° per minute in a homemade box furnace. The phase pure calcined powder is used for pelletization of the 10 mm circular disc and 1000 micron to 1500 micron thickness using the hydraulic machine under the pressure of $4-5\,N/m^2$. The green pellets were sintered at 900 °(±2 °) for densification and phase homogeneity. For electrical measurements, the circular disc of diameter 10 *mm* was cut into a cuboid structure of $10\,mm \times 4\,mm \times 1\,mm$. For the electrical connection and better charge accumulation during the change in humidity, a 3 mm × 4 mm × 1 mm silver cap was painted on both ends of the cuboid with the help of silver colloidal paint. Two copper wires were attached on the silver cap for the two probes current-voltage (IV) measurement. The device was placed on a self-designed bridge, where all six faces of the cuboids were equally exposed to the ambiance for proper humidity sensing.

2.1. Measurement and characterization

The polar resistive humidity sensor made of KTN ferroelectric polycrystalline ceramic was synthesized by the solid-state reaction technique. The X-ray diffractometer (RIGAKU-JAPAN/ULTIMA IV, λ = 1.5405 Å) with the monochromatic Cu-k_α radiation source in the range of 2θ, 20 to 80 °, was used to characterize the crystal structure and phase purity of the system. The XRD measurement was performed over the clean surface of the sensor with the step size 0.02 and scan rate 2° per minutes. The density of the device was measured using the Archimedes principle. The surface morphology and microstructural analysis of the sensor were performed by scanning electron microscopy (SEM, Zeiss EVO MA-10) technique. The Energy-dispersive X-ray spectroscopy (EDAX) was studied for the detail elemental composition analysis. The dielectric/ferroelectric measurements were carried out using Radiant ferroelectric tester at room temperature. The humidity sensor was characterized by the humidity generation and calibration equipment from thunder

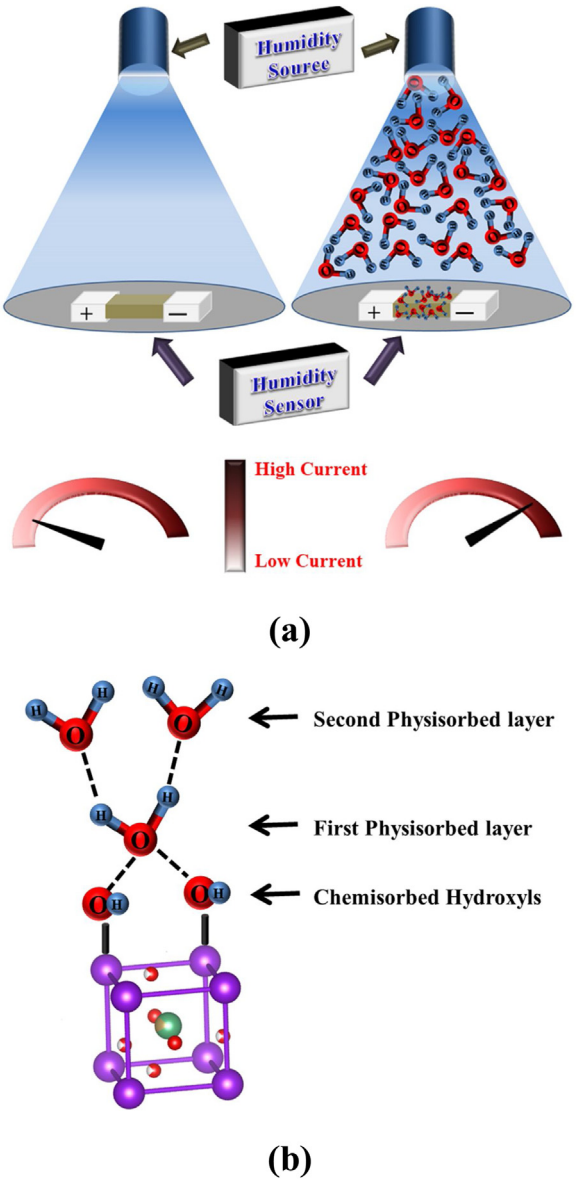

Fig. 1. (a) The pictorial representation of the adsorption of water molecules to the sensor interface and its effect on the current when the sensor is kept under dry (left image) and moist environment (right image). (b) The detailed explanation of the Grotthuss mechanism, the formation of chemisorbed and physisorbed layers and the interaction of hydroxyl (OH-) group with the metallic atom.

scientific corporation (The humidity source), Model 2500 Benchtop. The sensor was characterized at a different proportion of the relative humidity, i.e. 15%, 35%, 50%, 75%, and 95%, in adsorption and desorption mode. The electrical measurement of the humidity sensor was performed in two probe method with the help of Keithley-236 source meter. Various closed loop current-voltage (I /V) and current-time (I/T) measurement data were recorded by the LabView interfaced program with the Keithley-236. The schematic diagram and the mechanism responsible for giant humidity sensitivity in KTN polycrystalline are presented in Fig. 1 (a) and (b).

2.2. Rietveld refinement

The Rietveld refinement of the XRD data was carried out with the help of FULLPROF software package in the range of Braggs angle (2θ) 20° to 80° degree. The data was refined in the Structural Model (Rietveld Method) mode, under these conditions; all the param-

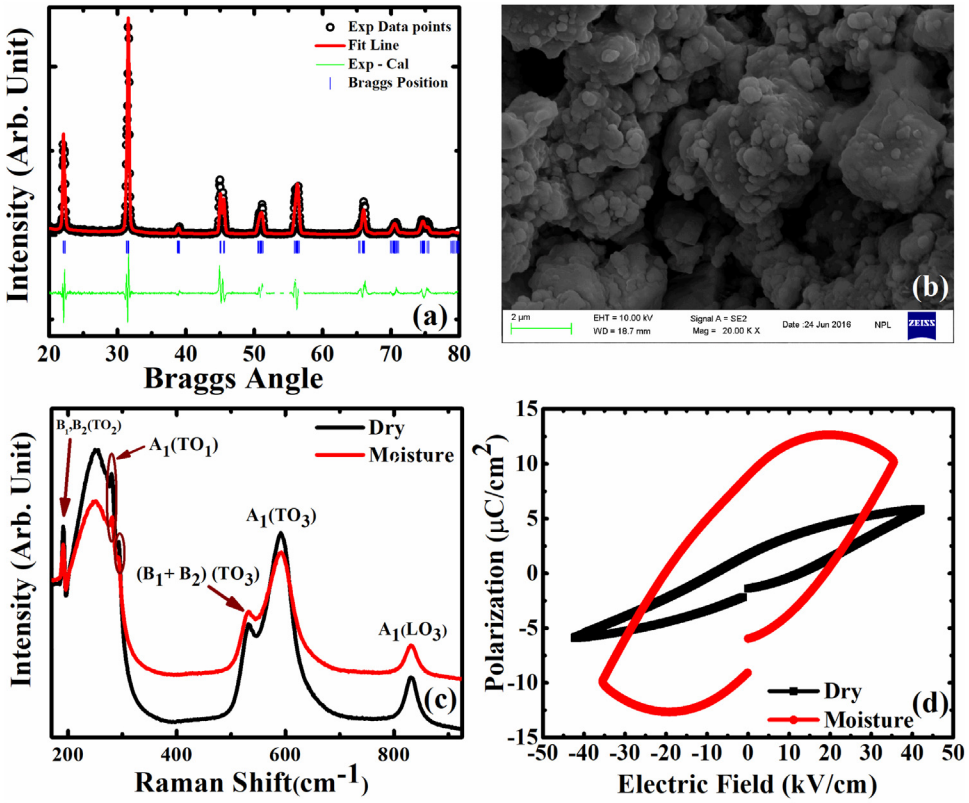

Fig. 2. (a) Rietveld refined X-ray diffraction patterns of the KTN ceramics. The experimental and Rietveld refined data are represented by an open circle and solid line, respectively. The vertical lines lie just below the peaks of XRD patterns represent the Bragg's planes of the KTN (b) SEM micrograph of the KTN shows the compactness and supports the low porosity of the sintered KTN pellet (i.e., 12%). (c) Raman spectrograph of the KTN sample in the dry and moist condition. (d) Enhancement of the electric polarization in the external applied an electric field, under the influence of the moisture (For interpretation of the references to colour in this figure legend, the reader is referred to the web version of this article).

eters including Wyckoff position were refined. The Background of the XRD data was fitted with the sixth order of the polynomial, and the peak positions were considered in Pseudo-Voigt Axial divergence asymmetry profile. In the Rietveld refinement thermal parameter, scale factor, lattice parameters, background, zero correction, and position coordinate were varied according to the appropriate requirement of the crystal structure, software, and for meaning full fitting. The occupancy of the ions was fixed during the refinement. The isotropic thermal parameters for all the ions continuously change to improve the R-factor. No such measure correction was observed to refine the thermal parameter with the position parameter and another parameter also.

3. Results and discussion

3.1. Structural and morphological study

Fig. 2 (a) shows the X-Ray diffraction (XRD) patterns of the polycrystalline KTN ceramic at room temperature (300 K). The KTN polycrystalline ceramic had the orthorhombic crystal structure with space group *Amm2*. All the diffraction planes were assigned with the orthorhombic crystal structure, matched with the JCPDS file number 71-0946 [19]. A distinct and sharp peak position illustrates the excellent crystal quality of the KTN polycrystalline ceramic. To study more about the crystal structure, the Rietveld refinement of the XRD data was carried out by considering the orthorhombic crystal structure and *Amm2* space group with the help of the FULLPROF software package. A single phase crystal structure was observed in the refinement. The Rietveld analysis confirms the doping of the Ta^{+5} at B-site of the perovskite ABO_3 crystal structure. There were total five elements present in the asymmetric crystal structure, in which, K (potassium) is on the 1(A) site, and Nb/Ta/Mn is on the 1(B) site of the ABO_3 crystal structure. The observed volume of the unit cell is 129.0022 cubic Å and the obtained R-factor (R), and reflection intensity based R-factor (R_f) from the refinement was 8.76, and 6.71, respectively. The refined lattice parameters of the crystal structure were $a = 3.9836\,Å$, $b = 5.6698\,Å$, *and* $c = 5.7116\,Å$. The goodness-of-fit, χ^2 (chi squire) was found to be 3.3 which suggested the goodness of the Rietveld refinement. Recently *Yasuhiro Yoneda et al.* described in detail about the local structure of the $KNbO_3$ at a different temperature, i.e., 15 K, 300 K, 673 K, and 1073 K and confirms about the orthorhombic crystal structure with phase group *Amm2* at room temperature. The present study of Rietveld analysis also shows the similar crystal structure parameters as reported earlier [20].

The cross-sectional SEM micrograph image of the sintered pellet was illustrated in Fig. 2(b). The SEM micrograph shows the oblate cuboid shape granular grains structure. The size of the cuboid grains lies from several 100 nm to few micrometers. The micrograph shows that a small spherical size particle is attached to the cuboid sized grain. The observed value of the porosity is 12%, which was measured by the Archimedes principle. The sintering temperature agglomerates the grains and decreases the porosity of the sensor; however low sintering temperature reduces the life cycles of the sensor materials. Moderately low porosity of the sensor supports high sensing ability with long lifetime and durability. Even for moderately low porosity, the sensor showed giant humidity sensing property. The presence of individual elements and its compositions were carried out by the EDAX technique on a large area at various positions on the sensor. The EDAX analysis provides evi-

dence of even distribution of elements with a composition similar to desired compositions well within the experimental error limit (±10 %) from all the sources.

3.2. Raman spectroscopy

Fig. 2 (c) illustrates the Raman spectroscopy image of the polycrystalline KTN sample at room temperature. Raman spectroscopy is vital to understand the structural disorder, phase evolution and different kind of ordering in the perovskite structure. The Raman spectra were recorded in two different modes; (i) dry condition, (ii) with Rh 95%. There were two sharp modes observed at 192 cm^{-1} and 296 cm^{-1} correspond to transverse optical mode 2 (TO_2) and transverse optical mode 4 (TO_4), respectively. These two modes are the fingerprint of occurrence for the long-range polar ordering in KTN ceramics [20,21]. In the high wavenumber region, the Raman longitudinal optical mode $A_1(LO_3)$ is associated with oxygen octahedra of perovskite. The peak splitting at the mid-range of Raman shift at 531 cm^{-1} and 591 cm^{-1} corresponds to (B_1+B_2) TO_3 and $A_1(TO_3)$, which confirms the orthorhombic crystal structure concerning *Amm2* space group [20,22]. These modes are assigned as per group theory [21–22]. Raman shift observed at 831.25 cm^{-1} and 293.75 cm^{-1} were correspond to the cross-linking of Nb^{+5} and K^+ cations with the octahedral oxygen ($^{16}O_8$). The full-width half maxima and peak sharpness corresponding to polar Raman modes (192 cm^{-1} and 293 cm^{-1}) decreased when Raman spectra were recorded with Rh 95%. These observations confirm the presence of a large number of active charge carriers surrounding to the oxygen octahedral which leads to significant distortion in crystal structure due to the participation of cations with an active hydroxyl group and hence, a large number of charge carriers present in the moist condition.

3.3. Polarization as a function of electric field in dry and wet condition

Fig. 2 (d) describes the behavior of electric polarization as a function of the electric field. The electric polarization of KTN sample was recorded at the room temperature in two different conditions; (i) in dry, (ii) in moisture condition. This measurement was performed to establish the effect of moisture on the ferroelectric nature of the KTN ceramic. The ferroelectric hysteresis loops were measured at room temperature and 100 Hz frequency. The dried unpoled KTN ceramics show a well saturated slim ferroelectric hysteresis loop with the saturation electric polarization 5.8 $\mu C/cm^2$. A well-shaped and saturated hysteresis under the maximum applied field 42 kV/cm confirms the ferroelectric nature of the dry KTN ceramics, however at the same time; the moist KTN shows leaky PE loops support the influences of freely conducting charge carriers on real polarization/displacement current. It has been explained earlier, that the shape of the PE loop described the various states of ferroelectric and dielectric materials [23–26]. Among them, one of the famous articles is Ferroelectrics go bananas by Prof. J F Scott [27].

3.4. Relative humidity and its mechanism

The relative humidity is the ratio of the amount of water vapor present in specific volume to the equilibrium water vapor at a given temperature. Mainly two types of parameters are used for the fabrication of humidity sensors available in the market; (i) the change in resistance and (ii) the change in dielectric constant or capacitance as a function of humidity. These parameters are employed to fabricate sensor output as a digital display unit. In the case of the resistance-based humidity sensor, if the sensor resistance increases with an increase in Rh%, it is called a positive response of resistance. Similarly, if the resistance of sensor decreases with an increase in

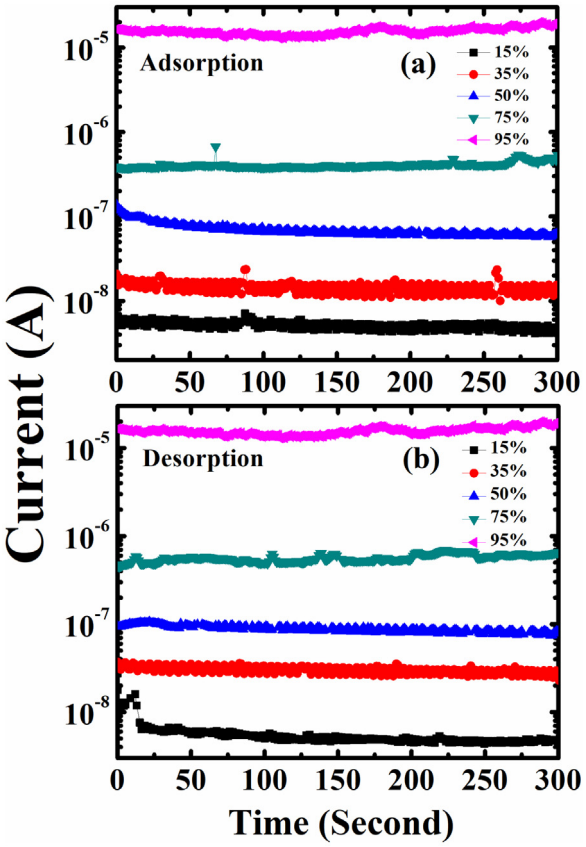

Fig. 3. The variation of the direct current at the different concentration of the relative humidity from 15% to 95% at 25°. The electric current is presented in the (a) adsorption, and (b) desorption mode.

Rh%, it is called a negative response of resistance [10,14,16,28–30]. In the present study, a negative response of humidity sensor is observed and utilized for fabrication of the display unit. The crystal structure, grains and grain boundaries distributions, homogenous microstructure, controlled porosity, and active participation with humidity make it a suitable candidate for an electrochemical reaction or giant sensing ability [28,31]. First, a water vapor molecule comes into the contact of activate surface of the sensor, i.e., adsorption of the water molecule, as explained in Fig. 1 (a). Consequently, hydrogen bonding becomes weaker and the water molecule transfers the hydroxyl group to the potassium atom as shown in Fig. 1 (b). The adsorption of the hydroxyl group to an activated potassium atom formed the chemisorbed layer. Now the water molecules from vapor make the hydrogen bonding with two nearby hydroxyl groups. This process formed the first physisorbed layer. The First physisorbed layer does not possess the hydrogen bonding itself, so there is no protonic conduction takes place at this level. Now the other water molecules start to bonding by hydrogen bonding and make the array upon the first physisorbed layer. These layers are called the second, third, fourth, and nth (layer) physisorbed layer as shown in Fig. 1 (b). Due to the presence of hydrogen bonding from the second physisorbed layer, Grotthuss mechanism comes into the picture which leads protonic conduction and hence may fold increase the conductivity of sensor with an increase in humidity [32–34].

3.5. Humidity sensing properties

The electrical properties of the KTN humidity sensor are described in Fig. 3 and Fig. 4. The humidity measurement was performed in the primary humidity standard placed at CSIR-National

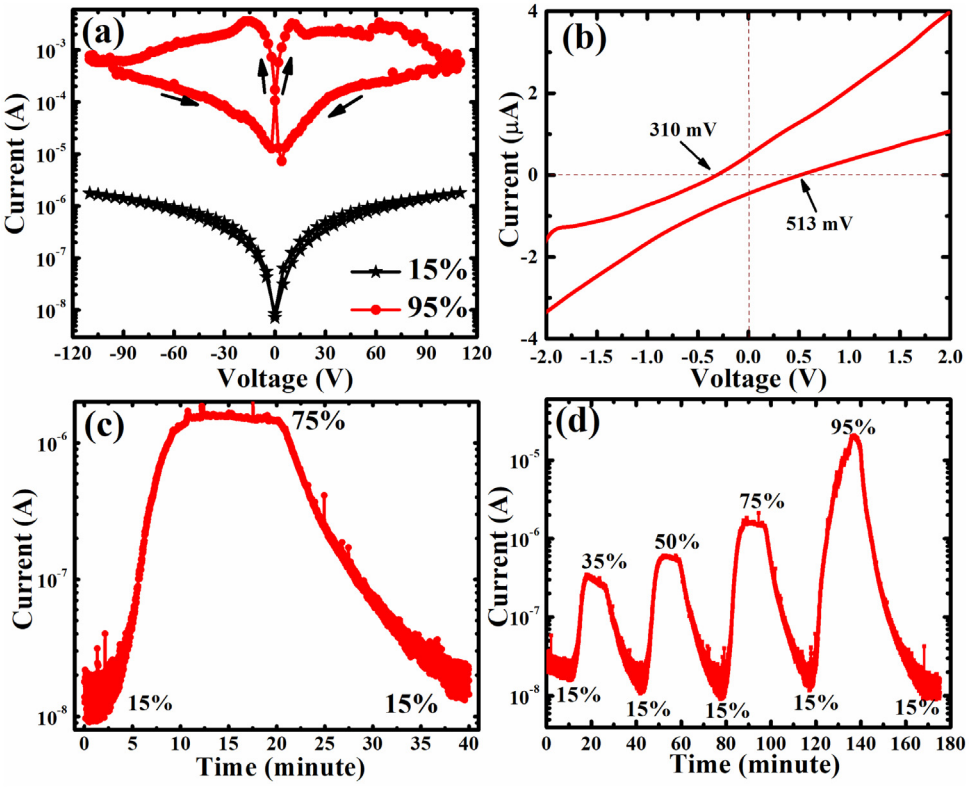

Fig. 4. (a) Closed loop current-voltage measurement of the sensor at two relative humidity concentration of 15% and 95%; the arrows show the current path as voltage swipe from negative to positive and positive to negative continuously. (b) the closed loop current-voltage graph in the range −2 V to +2 V with voltage span of +/- 10 V, shows the inbuild voltage of sensor in the range of 310 mV to 500 mV. (c) The performance of the sensor and the behavior of the current during the continuous variation of the relative humidity went from 15% to 75 % and returns to 15% (d) Variation of the current with the continuous switching of the relative humidity in the range of 15% to 95%.

Table 1
The variation of current and resistance as function of Rh% for both adsorption and desorption mode.

Relative Humidity (Rh)	Adsorption		Desorption	
	Current (A)	Resistance (M-Ω)	Current (A)	Resistance (M-Ω)
15 %	4.16E-9	1202.18	4.81E-9	1040.47
35 %	1.50E-8	332.55	2.35E-8	212.49
50 %	6.30E-8	79.33	8.11E-8	61.61
75 %	5.36E-7	9.33	6.49E-7	7.69
95 %	1.92E-5	0.26	1.92E-5	0.26

Physical Laboratory. Fig. 3 shows the variation in direct current of the sensor as a function of time at the constant applied voltage 5 volt. The variation of the current (related resistance) was recorded at the different value of the relative humidity (15% to 95%) during the adsorption and desorption mode. The three order change in current magnitude was observed with increase in humidity. The current value changes from a few nA to several μA with an increase in the humidity level from 15% to 95%, respectively depending on magnitude and direction of bias voltage. A detailed variation of electric current from 15% to 95% humidity level is given in Table 1. As the humidity increases, the number of physisorbed layers associated with the particular concentration of humidity increases which provide the colossal charge density, and a constant electric field provides the high mobility for the protonic conduction. For humidity level greater than Rh 50%, the presence of hydroxyl group increases faster which favors the exponential growth of electrical current with a change in humidity. It can be seen from Fig. 3 (a, b) that the presence of the hydroxyl group during physisorption and chemisorption process was all most constant, so KTN sensor provides the same overall range of the current during increasing and decreasing relative humidity (in different cycles of the measurement). It indicates that for the full range of the humidity, the interaction between the water molecule and microstructure of the KTN sensor continuously developed and destroyed the physisorption layers. The giant change in the electrical conductivity is caused by protonic conduction over the surface of the device. [28,32,35,36].

Fig. 4 (a) shows the closed loop current-voltage (I-V) scan with an applied voltage 110 V at two different humidity level 15% and 95%. The closed-loop covered the voltage scan from -110 V →0 V →+110 V to +110 V →0 V → -110 V, continuously. These measurements were performed to understand the behavior of the physisorption layer and how it behaves when the number of the physisorption layer increased. There is no current-voltage hysteresis observed in the closed loop I-V scan of the 15% humidity level. It shows that sensor surface forms only a few physisorbed layers, hence a very small amount of current with the water vapor at 15% Rh. There was a large hysteresis with inbuilt voltage (310 mV to 513 mV) at the humidity level of the 95%. It is interesting to note that humidity response abruptly changes with a change in the bias polarity/Voltage. Due to inbuilt potential, the sensor shows the switching of the current from negative to positive and vice versa before the bias voltage crosses the zero potential. This is due to the

hydroelectric cell nature of devices, where the self-generated voltage at high humidity ranges dictates the current as shown in Fig. 4. (b). For better clarity, a closed loop current-voltage (IV) data near to zero potential is shown in Fig. 4 (b). It shows nearly 513 mV open circuit voltage (V_{OCV}) and 0.5 μA short circuit current (I_{SCC}) during the scanning of voltage from negative to positive potential while 310 mV V_{OCV} and 0.5 μA I_{SCC} form positive to negative voltage scan (Fig. 4 (b)). These inbuilt voltages are shown by the sensor at the 95% humidity level and +/- 10 V scan period. The magnitude of V_{OCV} and I_{SCC} indicate that this device is capable to generate energy and electricity in the presence of humidity (hydroelectric cell) similar to photovoltaic current in the presence of light. This particular property of the sensor opens a new window for the future hydroelectric cell.

Fig. 4 (c) illustrates the continuous variation of the current when the humidity is changing from 15% to 75% and 75% to 15 % again at a 5 V bias voltage. The humidity source generated the humidity at the constant rate and reached the desired value up to 10-12 minutes. The 75% humidity was held for 10 minutes whereas the current was also constant during this time. As the humidity changed the current value also change continuously. These results support the reproducibility of sensor humidity sensing properties while adsorption and desorption process. The check the repeatability and reproducibility of sensing element, resistance/current property of the humidity sensor was checked from 15% to 35% and back to 15%, 15% to 50% and back to 15%, 15% to 75% and back to 15%, and 15% to 95% and back to 15%, respectively at the constant 5 V biased voltage as shown in Fig. 4 (d). These data support robust reproducibility of sensing element while various humidity conditions. Note that these data were taken by primary humidity standard which has experimental limitation to reach the desired humidity and de-humidity conditions.

The sensitivity, repeatability and the nature of the humidity hysteresis are the key constraints to understand the property of the sensor [35–38]. The sensitivity of the humidity sensor is defined by the ratio of the current $\frac{I_{Rh}}{I_{dry}}$, where the I_{Rh} is the current of the sensor at respected relative humidity, and the I_{dry} is the current at the 15% relative humidity level. The sensitivity of the KTN sensor is presented in Fig. 5 (a). The sensitivity graph follows a linear relationship up to 75% humidity level in the logarithmic graph. This shows the best performance of the sensor in the low humidity range. The maximum sensitivity of the device was around 4600 in adsorption and desorption mode for Rh 95%. As per our best knowledge, the magnitude of sensitivity is giant and far above than any reported value for bulk polycrystalline samples [10,14,35,37,38]. The sensitivity of the sensor was calculated in adsorption and desorption mode which provides the same range of sensitivity in various cycles of the measurement. The resistance as function of Rh% of KTN ceramics sensor was tested many times for the reproducibility, and possible uncertainty in the measurement is marked in the Fig.5 (b). It shows the resistance data with a proper error bar which has obtained from the standard deviation of five data points (Type A uncertainty). To investigate the sensor life sustainability, the electric current measurement was performed after 30 days periodically at different concentration of the relative humidity that found satisfactory well within the errors of the experimental range. To understand the hysteresis behavior of the sensor resistance as a function of Rh% (15% to 95%) is given in Fig. 5 (b); these data are used for fabrication of the digital display unit.

To display the humidity of the sensor environment, the essential electronics was indigenously developed. Since the sensitivity of the sensor was very high, so a simple electronics was unable to link with the sensor. The variation of the resistance in the sensor was converted into the output voltage signal with the help of inverting operational amplifier. The output signal of this operating amplifier

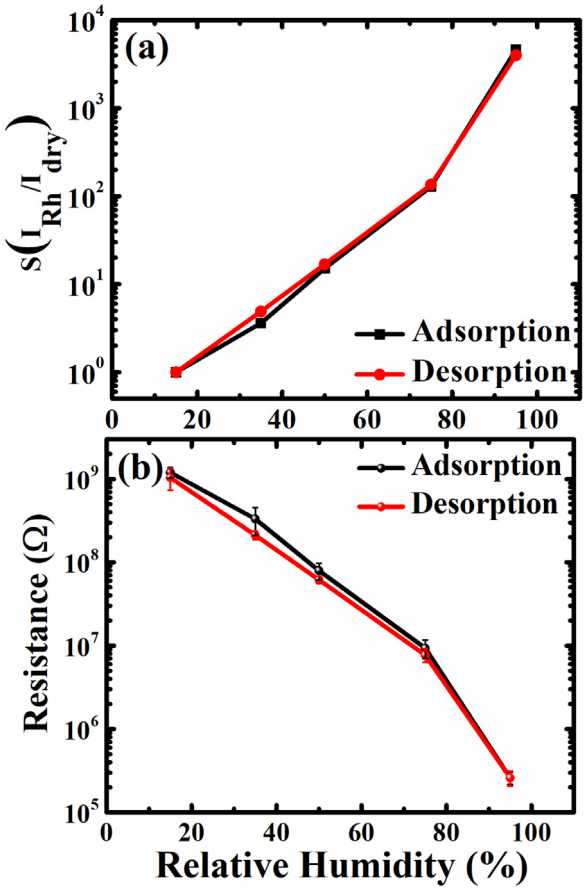

Fig. 5. (a) Describes the sensitivity $\left\{\frac{I_{Rh}}{I_{dry=15\%}}\right\}$ of the KTN sensor which comes out to be 4600 at 25°C (b) Resistance versus relative humidity hysteresis behavior of the KTN sensor having the uncertainty bar with respect to different humidity level.

was negative, so it was converted into the positive signal. The detail explanation of the electronics circuit was given in Fig. 6 (a) & (b). The constant positive bias voltage of 5 V to the sensor was maintained since pin 2 of the operational amplifier U1 was at virtually ground state. The KTN sensor shows giant sensitivity; hence a small variation of the humidity can change a lot in the output circuit. So, the positive output of the second operational amplifier U2 was further smoothened with the extra electronics circuit to slow down the variations in the signal. The output of the smoothing circuit was then applied to a suitable voltage measuring device which may be the low-cost microcontroller or a similar device such as a personal computer having an analog acquisition facility. The program written in the controller has the logic to convert the equivalent voltage into humidity. The resolution of humidity measurement depends on the capability of the analog measurement circuit or computer. The developed display unit with standard humidity sensor is shown in the supplementary data (Fig.S1).

4. Conclusion

We report the fabrication of low cost polar resistive polycrystalline KTN humidity sensor which displayed giant sensitive and long-term reproducibility. The resistance of the sensor changes from GΩ to several kΩ while changing the relative humidity from 15% to 95%. It illustrates an abrupt change in humidity sensing current with a change in polarity of bias voltage with large inbuilt voltage in the presence of high humidity. The giant variation of electrical current as a function of humidity and its micro-processing control suggest that the device will be a promising candidate for

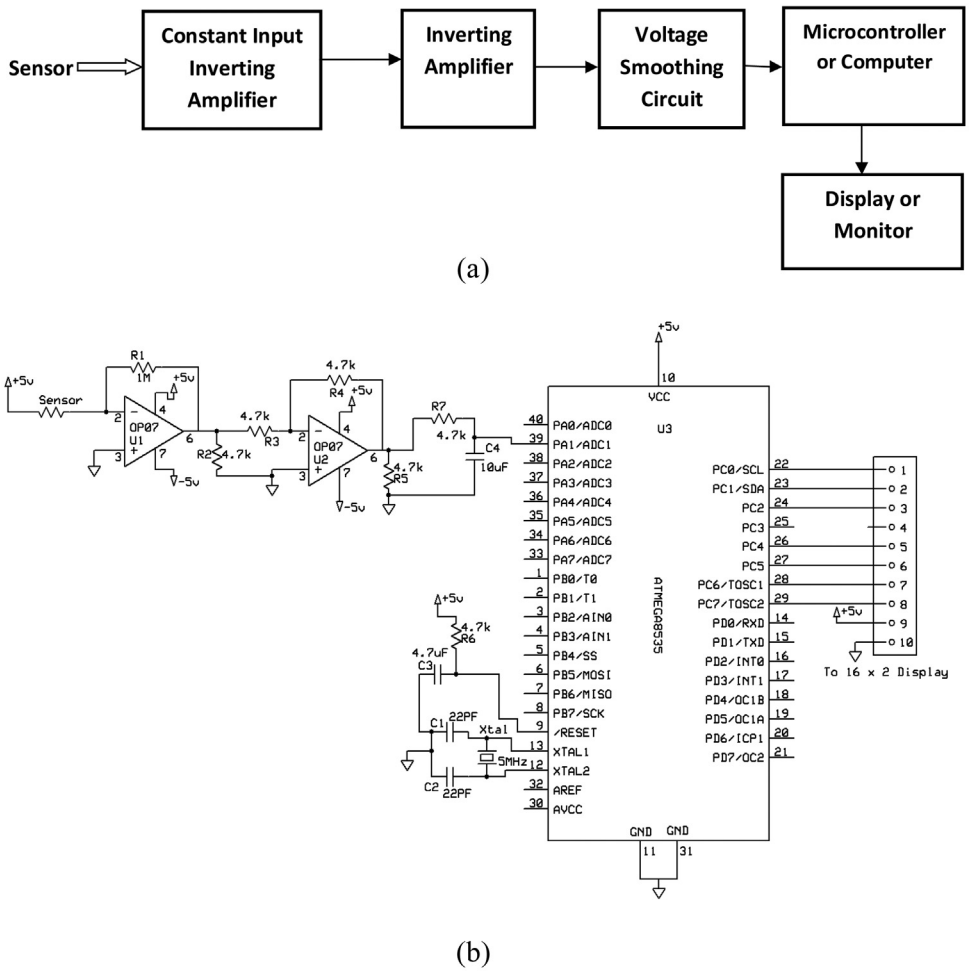

Fig. 6. (a) shows the detailed explanation of the electronic circuit in the flow chart. Fig.6 (b) shows the conversion of the resistance signal to the voltage signal, and again it is shown to display unit using the electronics circuit.

the practical humidity sensor. With the help of micro-electronics and digital display unit, the relative humidity is presented on the digital display unit. The present study revealed a new door for the low cost ultra-high sensitive sensors for the detection of humidity.

Acknowledgments

AK acknowledges the OLP180132 (CSIR project) for their financial assistant. Ravikant would like to acknowledge DST-INSPIRE to provide SRF fellowship to carry out the Ph.D. program.

Appendix A. Supplementary data

Supplementary material related to this article can be found, in the online version, at doi:https://doi.org/10.1016/j.sna.2019.05.023.

References

[1] Z. Li, H. Zhang, W. Zheng, W. Wang, H. Huang, C. Wang, A.G. MacDiarmid, Y. Wei, Highly sensitive and stable humidity nanosensors based on LiCl doped TiO_2 electrospun nanofibers, J. Am. Chem. Soc. 130 (2008) 5036–5037.
[2] R.E. Davis, G.R. McGregor, K.B. Enfield, Humidity: a review and primer on atmospheric moisture and human health, Environ. Res. 144 (2016) 106–116.
[3] Z. Chen, C. Lu, Humidity sensors: a review of materials and mechanisms, Sens. Lett. 3 (2005) 274–295.
[4] A. Merlone, G. Lopardo, F. Sanna, S. Bell, R. Benyon, R.A. Bergerud, F. Bertiglia, J. Bojkovski, N. Böse, M. Brunet, et al., The MeteoMet project - metrology for meteorology: challenges and results, Meteorol. Appl 22 (2015) 820–829.
[5] B. Buchholz, N. Böse, V. Ebert, Absolute validation of a diode laser hygrometer via intercomparison with the German national primary water vapor standard, Appl. Phys. B 116 (2014) 883–899.
[6] Y. Zhang, K. Yu, D. Jiang, Z. Zhu, H. Geng, L. Luo, Zinc oxide nanorod and nanowire for humidity sensor, Appl. Surf. Sci. 242 (2005) 212–217.
[7] H.Di Zhang, Y.Z. Long, Z.J. Li, B. Sun, C.H. Sheng, Synthesis, electrical and humidity sensing properties of $BaTiO_3$ nanofibers via electrospinning, Adv. Mater. Res. 418–420 (2011) 684–687.
[8] F. Liu, B. Quan, L. Chen, L. Yu, Z. Liu, Investigation on SnO2 nanopowders stored for different time and BaTiO3 modification, Mater. Chem. Phys. 87 (2004) 297–300.
[9] E. Dickey, O. Varghese, K. Ong, D. Gong, M. Paulose, C. Grimes, Room temperature ammonia and humidity sensing using highly ordered nanoporous alumina films, Sensors 2 (2002) 91–110.
[10] H. Bi, K. Yin, X. Xie, J. Ji, S. Wan, L. Sun, M. Terrones, Ultrahigh humidity sensitivity of graphene oxide, 2013, pp. 1–7.
[11] P.G. Su, C.F. Chiou, Electrical and humidity-sensing properties of reduced graphene oxide thin film fabricated by layer-by-layer with covalent anchoring on flexible substrate, Sens. Actuators B Chem. (2014).
[12] X. Liu, Y. Wen, B. Shan, K. Cho, Z. Chen, R. Chen, Combined effects of defects and hydroxyl groups on the electronic transport properties of reduced graphene oxide, Appl. Phys. A 118 (2015) 885–892.
[13] M. Parthibavarman, V. Hariharan, C. Sekar, High-sensitivity humidity sensor based on SnO2 nanoparticles synthesized by microwave irradiation method, Mater. Sci. Eng. C 31 (2011) 840–844.
[14] H.-E. Lin, Y. Katayanagi, T. Kishi, T. Yano, N. Matsushita, A solution-processed tin dioxide film applicable as a transparent and flexible humidity sensor, RSC Adv. 8 (2018) 30310–30319.
[15] Q. Kuang, C. Lao, Z.L. Wang, Z. Xie, L. Zheng, High-sensitivity humidity sensor based on a single SnO 2, Nanowire (2007) 6070–6071.
[16] D. Zhang, H. Chang, P. Li, R. Liu, Q. Xue, Fabrication and characterization of an ultrasensitive humidity sensor based on metal oxide/graphene hybrid nanocomposite, Sens. Actuators B Chem. 225 (2016) 233–240.
[17] G. Zhou, J.-H. Byun, Y. Oh, B.-M. Jung, H.-J. Cha, D.-G. Seong, M.-K. Um, S. Hyun, T.-W. Chou, Highly sensitive wearable textile-based humidity sensor

made of high-strength, single-walled carbon nanotube/poly(vinyl alcohol) filaments, ACS Appl. Mater. Interfaces 9 (2017) 4788–4797.
[18] J.-W. Han, B. Kim, J. Li, M. Meyyappan, Carbon nanotube based humidity sensor on cellulose paper, J. Phys. Chem. C 116 (2012) 22094–22097.
[19] R. Singh, P.K. Patro, A.R. Kulkarni, C.S. Harendranath, Synthesis of nano-crystalline potassium sodium niobate ceramic using mechanochemical activation, Ceram. Int. 40 (2014) 10641–10647.
[20] Y. Yoneda, K. Ohara, H. Nagata, Local structure and phase transitions of KNbO 3, Jpn. J. Appl. Phys. 57 (2018), 11UB07.
[21] J.A. Baier-Saip, E. Ramos-Moor, A.L. Cabrera, Raman study of phase transitions in KNbO3, Solid State Commun. 135 (2005) 367–372.
[22] W. Zhou, H. Deng, P. Yang, J. Chu, Structural phase transition, narrow band gap, and room-temperature ferromagnetism in [KNbO3]1−x[BaNi1/2Nb1/2O3−δ]x ferroelectrics, Appl. Phys. Lett. 105 (2014), 111904.
[23] H. Borkar, A. Kumar, Effects of light on ferroelectric polarization and leakage current, Vacuum 153 (2018) 91–95.
[24] P. Singh, H. Borkar, B.P. Singh, V.N. Singh, A. Kumar, Electro-mechanical properties of free standing micro- and nano-scale polymer-ceramic composites for energy density capacitors, J. Alloys Compd. 648 (2015) 698–705.
[25] M. Li, M.J. Pietrowski, R.A. De Souza, H. Zhang, I.M. Reaney, S.N. Cook, J.A. Kilner, D.C. Sinclair, A family of oxide ion conductors based on the ferroelectric perovskite Na0.5Bi0.5TiO3, Nat. Mater 13 (2014) 31–35.
[26] X. Qi, J. Dho, R. Tomov, M.G. Blamire, J.L. Macmanus-Driscoll, Greatly reduced leakage current and conduction mechanism in aliovalent-ion-doped, Cit. Appl. Phys. Lett 86 (2005) 62903.
[27] J.F. Scott, Ferroelectrics go bananas, J. Phys. Condens. Matter (2008).
[28] G.-C. Ri, J.-S. Kim, C.-J. Yu, Role of water molecules in enhancing the proton conductivity on reduced graphene oxide under high humidity, Phys. Rev. Appl. 10 (2018), 034018.
[29] T.-G. Kang, J.-K. Park, G.-H. Yun, H.H. Choi, H.-J. Lee, J.-G. Yook, A real-time humidity sensor based on a microwave oscillator with conducting polymer PEDOT:PSS film, Sens. Actuators B Chem. 282 (2019) 145–151.
[30] Z.S. Hosseini, A. Iraji zad, M.A. Ghiass, S. Fardindoost, S. Hatamie, A new approach to flexible humidity sensors using graphene quantum dots, J. Mater. Chem. C 5 (2017) 8966–8973.
[31] G. Young, Interaction of water vapor with silica surfaces, J. Colloid Sci. 13 (1958) 67–85.
[32] N. Agmon, The Grotthuss mechanism, Chem. Phys. Lett. 244 (1995) 456–462.
[33] Z. Chen, C. Lu, Humidity sensors: a review of materials and mechanisms, Sens. Lett. 3 (2005) 274–295.
[34] H. Farahani, R. Wagiran, M.N. Hamidon, Humidity Sensors Principle, Mechanism, and Fabrication Technologies: A Comprehensive Review, 2014, ISBN 6038946632.
[35] D. Burman, R. Ghosh, S. Santra, P.K. Guha, Highly proton conducting MoS 2 /graphene oxide nanocomposite based chemoresistive humidity sensor, RSC Adv. 6 (2016) 57424–57433.
[36] M. Zhong, Z. Wei, X. Meng, F. Wu, J. Li, Ultra-sensitive humidity sensors based on ZnSb 2 O 4 nanoparticles, RSC Adv. 5 (2015) 2429–2433.
[37] Z. Wang, L. Shi, F. Wu, S. Yuan, Y. Zhao, M. Zhang, The sol–gel template synthesis of porous TiO 2 for a high performance humidity sensor, Nanotechnology 22 (2011), 275502.
[38] G.-C. Ri, J.-S. Kim, C.-J. Yu, Role of water molecules in enhancing the proton conductivity on reduced graphene oxide under high humidity, Phys. Rev. Appl. 10 (2018), 034018.

Biographies

Ravikant received B.Sc. (HONOS) and M.Sc. degree in Physics at Hansraj College, University of Delhi, Delhi in 2012 and 2015, respectively. Currently, he is pursuing a Ph.D. in CSIR-National Physical Laboratory, New Delhi under the supervision of Dr. Ashok Kumar. His research field covers the area of multiferroics materials, sensors and superconductors, and memory devices.

Sheshamani Singh received the B.Sc. degree in St.Andrew's College Gorakhpur affiliated to D.D.U. Gorakhpur University, Gorakhpur in 2013. He received the M.Sc. degree from the Department of Physics, Amity School of Applied Sciences, Amity University Rajasthan, Jaipur in 2016. His research interests are in bulk and nanostructures multiferroics materials for non-volatile memory devices.

Gaurav Gupta obtained his M.Tech. in 2016 from MDU, Rohtak, and A.M.I.E. in 2010 from Institutions of Engineers (India) in Mechanical Engineering. Presently he is working as a technologist at CSIR-National Physical Laboratory, New Delhi. His current research interest is on humidity, dew point, and moisture studies.

Dr. Sanjay Yadav is a senior principal scientist in CSIR-National Physical Laboratory, New Delhi. He gained his Ph.D. degree in physics at Meerut University (Meerut, India) in 1990. Currently, he is working in the pressure metrology and divisional head of the pressure & Vacuum and ultrasonic metrology section in the CSIR-NPL. His research of interest is related to hydraulic pressure, barometric pressure, and related software development.

Dr. P. K. Dubey received a Ph.D. degree in ultrasonic instrumentations at R.T.M. Nagpur University, (Nagpur, India). Currently, he has held the Senior Scientist position in CSIR-National Physical Laboratory, New Delhi. His research of interest is electronics instrumentation, acoustic transducer, EMAT based non-contact NDT.

Dr. V.N. Ojha is a retired chief Scientist from CSIR-National Physical Laboratory, New Delhi. He received a Ph.D. degree in 1987 at University of Delhi. His area of research interest is Josephson series array voltage standard, 10 V- JVS system for dissemination of unit volt, low Tc superconductors and semiconductor devices, microwave device and fabrication of Photoelectric Pyrometer.

Dr. Ashok Kumar obtained a Ph.D. degree in physics at T. M. Bhagalpur University, Bhagalpur, Bihar (India) in 2005. He currently holds senior scientist position at CSIR-National Physical Laboratory, New Delhi. His research interest is ferroelectrics, multiferroics, photovoltaic, superlattices, high-k dielectrics, Inorganic-organic hybrid nanostructures, relaxors, high energy density supercapacitors, superconductor, spintronics, and ultra-high vacuum technology.